AIAA JOURNAL
Vol. 44, No. 2, February 2006

Prediction of Separated Flow Characteristics over a Hump

Vivek Krishnan* and Kyle D. Squires†
Arizona State University, Tempe, Arizona 85287-6106
and
James R. Forsythe‡
Cobalt Solutions, LLC, Springfield, Ohio 45504-3336

Predictions of the flow over a wall-mounted hump are obtained using solutions of the Reynolds-averaged Navier–Stokes (RANS) equations and detached-eddy simulation (DES). The upstream solution is characterized by a two-dimensional turbulent boundary layer with a thickness approximately half of the maximum hump thickness measured at a location about two chord lengths upstream of the leading edge. The Reynolds number based on the hump chord length is 9.75×10^5. A slot at approximately 65% chord C is used for flow control via a spatially uniform (with respect to the spanwise coordinate) steady suction and with alternating suction/blowing. Solutions of the two- and three-dimensional RANS equations are obtained using the Spalart–Allmaras (S-A) and shear-stress-transport (SST) turbulence models. DES is applied to a three-dimensional geometry corresponding to an extruded section of the hump. DES predictions of the baseline case exhibit a three-dimensional chaotic structure in the wake, with a mean reverse-flow region that is 20% shorter than predicted by the two-dimensional RANS computations and a mean reattachment length that is in good agreement with measurements. DES predictions of the pressure coefficient in the separated-flow region for the baseline case also exhibit good agreement with measurements and are more accurate than either the S-A or SST RANS results. The simulations also show that blockage effects in the experiments used to assess the predictions are important: three-dimensional RANS predictions more accurately predict the pressure distribution upstream and over the front portion of the hump. Predictions of the steady suction case show a reduction in the length of the reverse-flow region, though are less accurate compared to the baseline configuration. Unsteady two-dimensional RANS predictions of the sinusoidal suction/blowing case are used to investigate impedance affects associated with increases in the driving velocity. The simulations show that a factor of four increase in the cavity driving velocity increases the average velocity through the slot by only a factor of 2.7.

I. Introduction

THE development of computational tools that can be used to guide and optimize approaches for controlling complex flows at realistic Reynolds numbers comprises a topic of significant current interest. Various active flow control concepts such as pulsed jets,[1] piezoelectric actuators,[2] and zero-net-mass oscillatory actuators (synthetic jets)[3] have been investigated in flight and through lab experiments. Such experiments have often demonstrated that significant performance gains might be achieved through flow control. Computational fluid dynamics (CFD) offers a useful tool in understanding flow characteristics and studying the performance gains that can be achieved through flow control, although advances in several areas are needed to improve the robustness of CFD predictions for applications.

The flowfields for which control would be advantageous are complex: the flows are far from equilibrium, for example, separated or on the verge of separation, and distorted by effects such as strong pressure gradients and streamline curvature. This challenges simulation strategies because application Reynolds numbers are sufficiently high so that empirical input to any modeling procedure appears unavoidable. In addition, it is desirable in many flow control applications to apply a microscopic (e.g., small-scale) input and achieve a desired macroscopic (large-scale) output. This implies a wide range in the geometric scales to be simulated, which in turn can challenge aspects such as grid design and construction, possibly more so than in other CFD applications.

Most predictions for engineering applications are obtained from solution of the Reynolds-averaged Navier–Stokes (RANS) equations. RANS models yield predictions of useful accuracy in attached flows as well as some flows with shallow separation. In spite of this usefulness, RANS techniques typically fail to accurately predict complex flow structures in regimes substantially different from the thin shear layers used to calibrate the underlying turbulence models. Simulation strategies such as large-eddy simulation are attractive as an alternative for prediction of flowfields, where RANS is deficient but carries a prohibitive computational cost for resolving boundary-layer turbulence at high Reynolds numbers. This in turn provides a strong incentive for the merging of these techniques in hybrid RANS–large-eddy-simulation (LES) approaches.

Detached-eddy simulation (DES) is among the actively applied hybrid RANS–LES strategies.[4] The method aims at entrusting the boundary layer to RANS while the detached eddies in separated regions are resolved using LES. DES thus attempts to capitalize on the advantages of RANS and LES and in design applications, the RANS region of a DES comprises the entire boundary layer with the remainder of the flow, that is, the LES region, treated using a subgrid model. Predictions of the massively separated flows for which the technique was originally designed are typically superior to that which can be achieved using RANS models, especially of three-dimensional and time-dependent features (e.g., see Ref. 5 and references therein).

The objectives of the current effort are to apply and assess predictions using RANS and DES of a configuration with and without flow control, which poses a significant challenge to predictive strategies. The particular focus of the work is the calculations of the flow over a wall-mounted hump. The configuration is a Glauert–Goldschmied-type body and corresponds to case 3 from the recent

Presented as Paper 2004-2224 at the AIAA 2nd Flow Control Conference, Portland, OR, 28 June–1 July 2004; received 31 August 2004; revision received 23 June 2005; accepted for publication 23 June 2005.

*Graduate Research Associate, Mechanical and Aerospace Engineering Department. Student Member AIAA.
†Professor, Mechanical and Aerospace Engineering Department. Member AIAA.
‡Director of Research, 4636 New Carlisle Pike. Senior Member AIAA.

NASA Workshop on CFD Validation of Synthetic Jets and Turbulent Separation Control.[6] In the experiment, the hump model was mounted on a splitter plate between two glass endplates. Both the leading and trailing edges are smoothly faired to the solid walls upstream and downstream of the hump; the chord length is nearly eight times the value of the maximum hump thickness. The boundary layer experiences an adverse pressure gradient upstream of the hump, accelerates over the front convex portion of the body, and separates over a relatively short concave section in the aft region. A small slot extending across the entire length of the span and located at approximately 65% of the hump chord is used to introduce flow control, using either steady suction or sinusoidal suction/blowing. Detailed measurements were acquired for a baseline configuration (no flow control) in addition to the controlled cases.

Predictions of the steady-state flow are obtained via solution of the two- and three-dimensional RANS equations. Predictions of the three-dimensional and time-dependent flow are obtained using DES. The RANS predictions are obtained using the Spalart–Allmaras[7] and shear-stress-transport (SST)[8] turbulence models. Calculations of the two-dimensional flows correspond, nominally, to the central section of the wind tunnel. Three-dimensional effects can be subtle and possibly important in separated flows, even those that are designed and anticipated to be nominally two dimensional in the central section of the wind tunnel as is the case for the present study. Sidewalls that might exert an effect on the flow in wind tunnels, for example, through sidewall separations, are one example of the complexities that cannot be accounted for a priori in two-dimensional calculations. Thus, although two-dimensional simulations provide useful guidance for several factors such as grid densities, exploration of the influences of various boundary conditions, and an examination of the influence of turbulence models, corroboration of two-dimensional predictions using three-dimensional calculations, especially for separated flows, is essential. In the current effort, RANS predictions of the three-dimensional configuration include the wind-tunnel sidewalls and endplates. As shown next, accounting for their confining effects is crucial to accurately predicting the pressure distribution over the hump to the point of separation. The DES predictions are of a subset of the test section: a three-dimensional configuration produced by extruding the cross section of the model into the spanwise direction.

A side view of the hump geometry considered in the simulations is shown in Fig. 1. The hump is smoothly faired to the solid walls upstream and downstream of the leading and trailing edges. In the experiments,[6] the characteristic length is the hump chord $C = 0.42$ m. The maximum thickness of the hump is 0.054 m, corresponding to a chord-to-thickness ratio of 7.81. The tunnel dimensions at the test section were 0.71 m wide × 0.51 m high. The hump model was mounted on a splitter plate resulting in a nominal test-section height of 0.382 m (distance from the splitter plate to the top wall).

As shown in Fig. 2, a cavity is included in the computational representation of the hump. A slot at approximately $x/C = 0.65$, where the streamwise origin of the coordinate system coincides with the hump leading edge, is used to apply control via steady suction or sinusoidal suction/blowing, applied uniformly across the spanwise dimension of the configuration. For the case with steady suction, a constant mass flux is prescribed through the lower cavity opening. For the case with sinusoidal variation in the suction/blowing, the frequency of the mass flux exiting/entering the lower cavity surface was the same as in the experiments, that is, 138.5 Hz, and

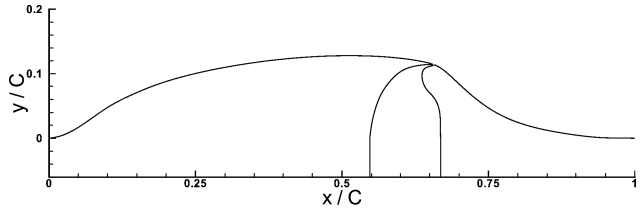

Fig. 1 Outline of the surface-mounted hump configuration.

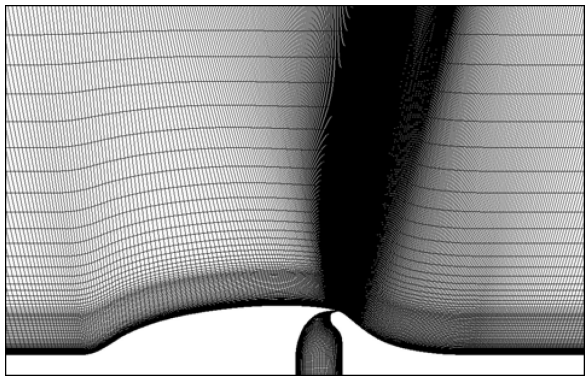

a)

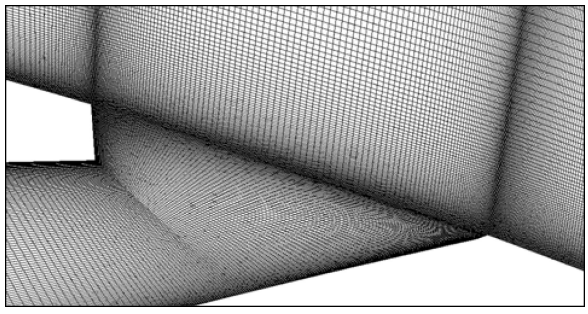

b)

Fig. 2 Side view of the structured mesh, 841 × 217 cells: a) grid in the vicinity of the hump (the entire extent of the vertical dimension is shown) and b) zoomed view of the grid in the vicinity of the slot used for simulations with suction/blowing.

with the mass flux along the lower cavity surface prescribed such that the maximum velocity through slot during the blowing phase of the cycle was approximately 26.6 m/s. (This condition corresponds to an oscillatory blowing momentum coefficient of approximately 0.111%.) The reader is referred to the summary of the experiments reported by Rumsey et al.[6] for further details.

The computational domain extends $6.39C$ upstream of the hump leading edge, sufficient to allow the growth of a turbulent boundary layer having a thickness close to the measured value of about 1.1 in. at a location $2.14C$ upstream of the leading edge as reported in the experiments. The total streamwise length of the computational domain is $12.74C$, with the domain extending $5.35C$ downstream of the hump trailing edge. The wall-normal extent of the domain extends $0.91C$ from the lower horizontal surface, identical to the corresponding dimension to the upper wind-tunnel wall in the experiments. The coordinate system origin is fixed to the leading edge with x aligned with the freestream (parallel to the lower flat wall), y normal to the horizontal lower wall, and z completing the right-hand rule.

II. Turbulence Models

RANS predictions are obtained using two turbulence models: the Spalart–Allmaras one-equation model[7] (referred to as S-A throughout) and the two-equation SST model of Menter.[8] All of the calculations summarized next are of fully turbulent flows, that is, with turbulent boundary layers initiated along all solid surfaces of the computational domain.

A. Spalart-Allmaras

The Spalart–Allmaras RANS model solves an equation for the variable $\tilde{\nu}$, which is dependent on the turbulent viscosity.[7] The model is derived based on empiricism and arguments of Galilean invariance, dimensional analysis, and dependence on molecular viscosity. The model includes a wall destruction term that reduces the turbulent viscosity in the laminar sublayer and trip terms to provide smooth transition to turbulence. The trip terms were not used in the present

investigations and are therefore not included in the following summary. The transport equation for the working variable $\tilde{\nu}$ used to form the eddy viscosity is written as

$$\frac{\mathrm{D}\tilde{\nu}}{\mathrm{D}t} = c_{b1}\tilde{S}\tilde{\nu} - c_{w1}f_w\left[\frac{\tilde{\nu}}{d}\right]^2 + \frac{1}{\sigma}\left\{\nabla\cdot[(\nu+\tilde{\nu})\nabla\tilde{\nu}] + c_{b2}(\nabla\tilde{\nu})^2\right\} \tag{1}$$

where $\tilde{\nu}$ is the working variable. The eddy viscosity $\mu_t = \rho\nu_t$ is formed via

$$\nu_t = \tilde{\nu}f_{v1}, \qquad f_{v1} = \chi^3\Big/\left(\chi^3 + c_{v1}^3\right), \qquad \chi \equiv \tilde{\nu}/\nu \tag{2}$$

where ν is the molecular viscosity. The production term is expressed as

$$\tilde{S} \equiv S + (\tilde{\nu}/k^2d^2)f_{v2}, \qquad f_{v2} = 1 - \chi/(1+\chi f_{v1}) \tag{3}$$

where S is the magnitude of the vorticity. The function f_w is given by

$$f_w = g\left[\frac{1+c_{w3}^6}{g^6+c_{w3}^6}\right]^{\frac{1}{6}}, \qquad g = r + c_{w2}(r^6 - r), \qquad r \equiv \frac{\tilde{\nu}}{\tilde{S}k^2d^2} \tag{4}$$

with large values of r truncated to 10. The wall boundary condition is $\tilde{\nu} = 0$. The constants are $c_{b1} = 0.1355, \sigma = \frac{2}{3}, c_{b2} = 0.622, \kappa = 0.41$, $c_{w1} = c_{b1}/\kappa^2 + (1+c_{b2})/\sigma$, $c_{w2} = 0.3$, $c_{w3} = 2$, and $c_{v1} = 7.1$.

B. Shear-Stress Transport

The shear-stress-transport (SST) model was developed by Menter[8] to improve the accuracy of the k–ω model for prediction of separated flows. The baseline version combines k–ε and k–ω formulations, using a parameter F_1 to bridge from k–ω near the wall to k–ε in the freestream. The transport equations governing k and ω take the form

$$\frac{\mathrm{D}\rho k}{\mathrm{D}t} = \tau_{ij}\frac{\partial u_i}{\partial x_j} - \beta^*\rho\omega k + \frac{\partial}{\partial x_j}\left[(\mu+\sigma_k\mu_t)\frac{\partial k}{\partial x_j}\right] \tag{5}$$

$$\frac{\mathrm{D}\rho\omega}{\mathrm{D}t} = \frac{\gamma\rho}{\mu_t}\tau_{ij}\frac{\partial u_i}{\partial x_j} - \beta\rho\omega^2 + \frac{\partial}{\partial x_j}\left[(\mu+\sigma_\omega\mu_t)\frac{\partial\omega}{\partial x_j}\right] + 2\rho(1-F_1)\sigma_{\omega2}\frac{1}{\omega}\frac{\partial k}{\partial x_j}\frac{\partial\omega}{\partial x_j} \tag{6}$$

where τ_{ij} is the (modeled) turbulent shear stress. The switching function F_1 is given by

$$F_1 = \tanh\left(\arg_1^4\right) \tag{7}$$

$$\arg_1 = \min\left[\max\left(\frac{\sqrt{k}}{0.09\omega y}; \frac{500\mu}{\rho\omega y^2}\right); \frac{4\rho\sigma_{\omega2}k}{CD_{k\omega}y^2}\right]$$

$$CD_{k\omega} = \max\left[2\rho\sigma_{\omega2}\frac{1}{\omega}\frac{\partial k}{\partial x_i}\frac{\partial\omega}{\partial x_i}; 10^{-20}\right] \tag{8}$$

The switching function F_1 is also used to determine the values of the model constants. If ϕ_1 represents a generic constant in the k–ω equations and ϕ_2 represents the same constant in the k–ε equations, then the model constants employed in Eqs. (5) and (6) are determined by

$$\phi = F_1\phi_1 + (1-F_1)\phi_2 \tag{9}$$

In the baseline version of the model, the turbulent eddy viscosity is determined as $\mu_t = \rho k/\omega$. The SST model limits the turbulent shear stress to $\rho a_1 k$, where $a_1 = 0.31$. This in turn leads to an expression for the eddy viscosity,

$$\mu_t = \frac{\rho a_1 k}{\max(a_1\omega; \Omega F_2)} \tag{10}$$

where Ω is the absolute value of vorticity. The function F_2 is included to recover the original formulation of the eddy viscosity for free shear layers

$$F_2 = \tanh\left(\arg_2^2\right), \qquad \arg_2 = \max\left(2\frac{\sqrt{k}}{0.09\omega y}; \frac{400\nu}{y^2\omega}\right) \tag{11}$$

The k–ω model constants are given by $\sigma_{k1} = 0.85$, $\sigma_{\omega1} = 0.5$, $\beta^* = 0.09$, $\beta_1 = 0.0750$, $\gamma = \beta_1/\beta^* - \sigma_{\omega1}\kappa^2/\sqrt{\beta^*}$, and $\kappa = 0.41$. The values of the k–ε model constants are $\sigma_{k2} = 1.0$, $\sigma_{\omega2} = 0.856$, $\beta_2 = 0.0828$, $\beta^* = 0.09$, $\gamma_2 = \beta_2/\beta^* - \sigma_{\omega2}\kappa^2/\sqrt{\beta^*}$, and $\kappa = 0.41$.

C. Detached-Eddy Simulation

The DES formulation is obtained by replacing in the S-A model the distance to the nearest wall d, by $\tilde{d}$, where $\tilde{d}$ is defined as

$$\tilde{d} \equiv \min(d, C_{\mathrm{DES}}\Delta), \qquad C_{\mathrm{DES}} = 0.65 \tag{12}$$

In Eq. (12), Δ is the largest distance between the cell center under consideration and the cell center of the neighbors (those cells sharing a face with the cell in question). The location where $\tilde{d}$ is determined by the grid spacing, that is, $\tilde{d} = C_{\mathrm{DES}}\Delta$, defines the interface between the RANS region and the LES region. In applications for which the wall-parallel grid spacings (e.g., streamwise and spanwise) are on the order of the boundary-layer thickness, the RANS region comprises most or all of the boundary layer, and the closure applied is the S-A RANS model. In the LES region the closure is a one-equation model for the subgrid-scale eddy viscosity. While natural applications of DES treat the entire boundary layer in RANS mode, grid refinement in the wall-parallel directions (both streamwise and spanwise) will cause the RANS–LES interface to move nearer the wall, activating the DES limiter and reducing the eddy viscosity below its RANS levels. This process can degrade predictions if mesh densities are insufficient to support eddy content within the boundary layer, resulting in lower Reynolds-stress levels compared to that provided by the RANS model.[4] For the present configuration, the adverse pressure gradient upstream of the hump thickened the boundary layer. That feature combined with the mesh spacings for the current grids caused the RANS–LES interface to reside sufficiently within the boundary layer such that the upstream flow prediction was altered compared to that obtained using the RANS models. To provide an evaluation of the DES predictions against the RANS for nominally similar upstream conditions, RANS behavior was maintained to a position slightly upstream of the slot, that is, $\tilde{d} = d$ for $x/C < 0.65$, with DES allowed to take effect downstream of this location.

III. Simulation Overview

A. Summary of the Cases

The computations performed for each of the three cases, baseline (no flow control), steady suction, sinusoidal suction/blowing, are summarized in Tables 1–3, respectively. Each table reports the grid sizes, grid topology, whether the computation was two or three dimensions, the boundary conditions, and turbulence models employed for a given simulation (the X in the table indicating the simulation was performed). The nomenclature in the tables for the grid topology indicates the mesh was structured or unstructured and with additional details for the three-dimensional computations as summarized next. The nomenclature for the boundary conditions "slip top wall" indicates a slip condition was applied to the upper surface of the computational domain, "bl top wall" indicates a boundary layer grid on the top wall and that the no-slip condition was applied, and "bl all walls" indicates boundary-layer grids on all walls of a three-dimensional computation and the imposition of no-slip conditions on all solid surfaces. Although results from each of the computations summarized in the tables are not presented in this manuscript, a more detailed summary is available in Rumsey et al.[6]

The predictions of the baseline case were performed using configurations that meshed the cavity and slot, though with the lower (horizontal) cavity surface closed. The steady-suction case imposed

Table 1 Summary of the computations of the baseline (no flow control) case

Dimension	Grid size	Grid topology	Boundary conditions	RANS S-A	RANS SST	DES S-A
2	421×109	Structured	Slip top wall	X	X	——
	841×101	Structured	Slip top wall	X	X	——
	841×217	Structured	Slip top wall	X	X	——
	841×257	Structured	Slip top wall	X	——	——
	841×257	Structured	Bl top wall	X	——	——
	890×257	Structured	Bl top wall	X	——	——
	1.14×10^5	Unstructured	Slip top wall	X	——	——
	2.47×10^5	Unstructured	Slip top wall	X	——	——
3	$841 \times 101 \times 41$	Structured, periodic	Slip top wall	——	——	X
	2.59×10^6	Unstructured, half-geometry	Bl all walls	X	——	——
	4.90×10^6	Unstructured, half-geometry	Bl all walls	X	X	——
	10.72×10^6	Unstructured, half-geometry	Bl all walls	X	——	——

Table 2 Summary of the computations of the steady-suction case

Dimension	Grid size	Grid topology	Boundary conditions	RANS S-A	RANS SST	DES S-A
2	421×109	Structured	Slip top wall	X	X	——
	841×101	Structured	Slip top wall	X	X	——
	841×217	Structured	Slip top wall	X	X	——
3	$841 \times 101 \times 41$	Structured, periodic	Slip top wall	——	——	X
	4.90×10^6	Unstructured, half-geometry	Bl all walls	X	X	——

Table 3 Summary of the computations of the blowing and suction case: two dimensions

Grid size	Grid topology	Boundary conditions	RANS S-A	Mass flux, kg/s
841×101	Structured	Slip top wall	X	0.0179
841×101	Structured	Slip top wall	X	0.0140
841×101	Structured	Slip top wall	X	0.0210
841×101	Structured	Slip top wall	X	0.0280
841×101	Structured	Slip top wall	X	0.0560

a fixed mass flux of 0.01518 kg/s (in the two-dimensional computations the mass flux was divided by the 0.584-m span of the slot through which suction was applied in the experiments) along the entire lower cavity surface. The zero-net-mass-flux oscillatory suction/blowing was performed by prescribing a sinusoidal variation in the mass flux exiting/entering the lower cavity surface. The suction/blowing frequency was 138.5 Hz. A series of simulations was performed in order to deduce the required peak in the mass flux at the cavity opening to yield a slot velocity during the blowing phase of 26.6 m/s, corresponding to the case measured in experiments. The first entry in Table 3, a mass flux of 0.0179 kg/s, was the value employed in the simulations and corresponding to the measured case. As also shown in Table 3, additional suction/blowing rates were applied to investigate the characteristics of the jet velocity through the slot and impedance effects associated with large blowing coefficients.

For each simulation, the reference conditions corresponded to standard atmosphere. At the outlet of the computational domain, the pressure was prescribed at 101,325 Pa, the reference temperature was 288 K, and the corresponding density was specified using the ideal-gas law. The reference Mach number was 0.1, leading to a Reynolds number per unit of length of 5.899×10^4, which yields a chord-based Reynolds number of 9.75×10^5.

B. Flow Solver, Grids, and Time Steps

The compressible Navier–Stokes equations are solved by using Cobalt. The numerical method is a cell-centered finite volume approach applicable to arbitrary cell topologies (e.g, hexahedra, prisms, tetrahedra) and described in Strang et al.[9] The spatial operator uses the exact Riemann solver of Gottlieb and Groth,[10] least-squares gradient calculations using QR factorization to provide second-order accuracy in space, and total-variation-diminishing flux limiters to limit extremes at cell faces. A point-implicit method using analytic first-order inviscid and viscous Jacobians is used for advancement of the discretized system. For time-accurate computations, a Newton subiteration scheme is employed; the method is second-order accurate in time. The domain decomposition library ParMETIS[11] is used for parallel implementation and provides optimal load balancing with a minimal surface interface between zones. Communication between processors is achieved using message passing interface.

The influence of mesh density and grid topology was investigated using a series of calculations on structured and unstructured grids. The influence of the boundary condition applied to the upper surface of the computational domain was also investigated. Each of the unstructured grids and the structured grids employed in the two-dimensional RANS calculations composed of 421×109 cells and 841×217 cells were generated by Rumsey et al.[6] A view of the finer mesh in the vicinity of the hump is shown in Fig. 2, illustrating the clustering of points in the vicinity of the slot. Three additional structured grids were also employed in the two-dimensional RANS study. The mesh composed of 841×101 cells was created using Gridgen, by coarsening the 841×217 mesh in the wall-normal direction. This grid was created in order to provide a more efficient mesh for subsequent DES calculations that extruded the geometry into the span. The remaining structured grids (841×257 cells and 890×257 cells) applied a no-slip condition to the upper surface of the computational domain, using finer meshes near the upper surface to resolve the boundary layers.

With the exception of the grid composed of 890×257 cells, the upstream section of the computational domain extended 6.39 chords forward of the hump leading edge. The simulation domain for the case with the grid size 890×257 extended 10.64 chord lengths upstream of the leading edge. The purpose of the computation was to investigate the influence of the thicker upper-wall boundary layer on the pressure distribution over the lower surface (on which the hump is mounted). Along the lower surface of the domain from 10.64 to 6.39 chord lengths, a slip condition was applied, with a no-slip condition applied at the streamwise location 6.39 chord lengths upstream of the hump leading edge. This in turn allowed the boundary layer to develop from the same upstream

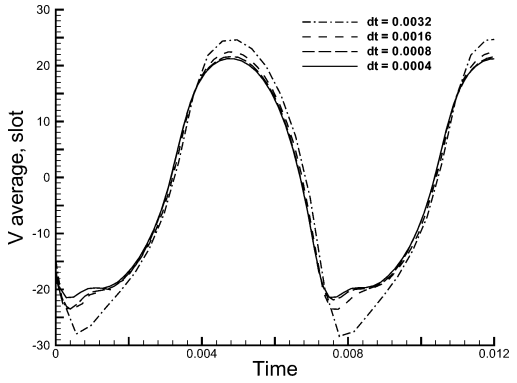

Fig. 3 Influence of the time step on the average slot velocity for the case with sinusoidal suction/blowing. Time steps are made dimensionless using hump chord length and freestream velocity.

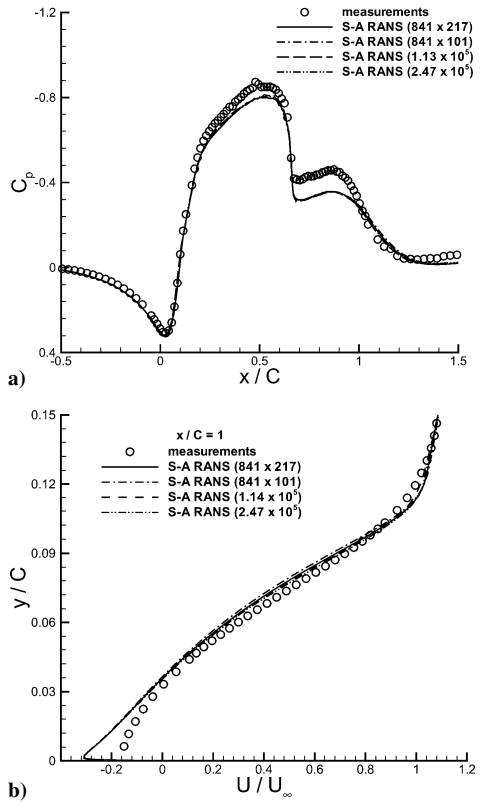

Fig. 4 Effect of mesh resolution and mesh type (structured or unstructured) on a) pressure coefficient and b) streamwise mean velocity profiles at $x/C = 1.0$.

location as the other simulations. Though not shown here, the influence of the longer upstream extent did not result in significant differences in RANS predictions compared to those presented next.

All RANS predictions of the baseline and steady-suction cases are of the steady-state flow. The governing equations were integrated using large time steps, corresponding to a Courant–Friedrichs–Lewy number (CFL) $= 10^6$. The predictions of the pulsed suction/blowing case were time accurate. Based on the results of a time-step study (Fig. 3), the time step for the blowing/suction case, nondimensionalized by the hump chord length and freestream velocity, was 8×10^{-4} (1×10^{-5} s). The mass flux values in Table 3 correspond to the peak values.

A representative sampling of the influence of the mesh on the two-dimensional RANS predictions is shown in Fig. 4. Plotted in the figure are the pressure coefficient and mean velocity profile at $x/C = 1.0$ using two structured grids and two unstructured grids. The measurements of the pressure coefficient show the development of the adverse pressure gradient prior to the leading edge of the hump, the acceleration of the flow to $x/C \approx 0.5$, and relatively strong adverse pressure gradient that develops prior to the location of flow detachment at $x/C \approx 0.65$. For the S-A RANS predictions shown in the left frame of Fig. 4, the length of the recirculation bubble extends approximately $0.63C$ downstream of separation. The right frame of the figure showing the streamwise mean velocity profile illustrates that the station $x/C = 1.0$ is within the reverse-flow region. The figure shows that for each grid topology, structured and unstructured, there is insignificant variation in both the pressure coefficient and streamwise mean velocity at $x/C = 1.0$ with more than a doubling in the number of cells for both the structured and unstructured grids. Assessment of the pressure coefficient and velocity profiles from the three-dimensional RANS predictions also exhibited grid convergence.

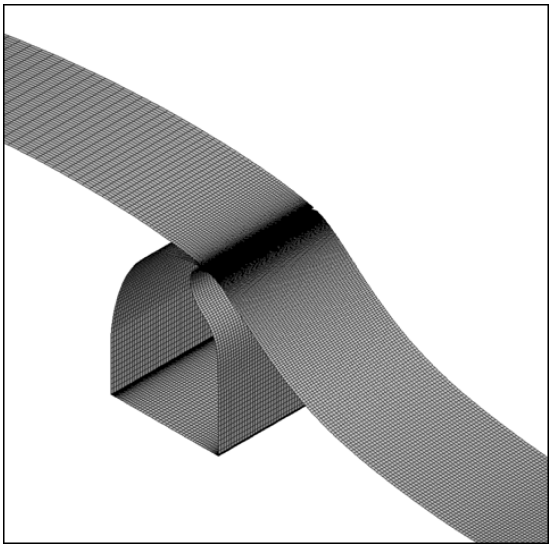

Fig. 5 Surface grid for the DES. Spanwise extent of the domain is $0.121C$, extruded into the spanwise coordinate with a uniform grid spacing of 0.00127 m.

The parameters of the DES summarized in Tables 1 and 2 corresponded to prediction of the flow over a section of the hump. The grid with 841×101 cells (and used in the RANS calculations as just summarized) was extruded into the spanwise direction to create the three-dimensional geometry. The spanwise dimension was meshed using 41 points with an equal spacing of 0.00127 m, leading to a spanwise period of 0.121 chord lengths (Fig. 5). This grid spacing leads to a resolution of approximately 20 points per boundary-layer thickness in the wall-parallel directions (based on the reference location upstream of the leading edge) and also yields approximately cubic cells in the separated region downstream of the slot. Periodic boundary conditions were applied along the spanwise direction, indicated by the reference "structured, periodic" in the grid topology entry in the tables.

A time-step study was performed using the DES prediction of the baseline configuration (no flow control). Dimensional time steps of 2×10^{-5}, 4×10^{-5}, and 8×10^{-5} s (corresponding to dimensionless values of 0.0016, 0.0032, and 0.0064, where the flow timescale is defined using the hump chord length and freestream velocity) were employed, the intermediate time step yielding a CFL around unity in the focus region corresponding to the recirculating region downstream of the hump.[12] Figure 6 shows the three locations, $x/C = 0.8$, 0.92, and 1.04, at which time series were extracted for calculation of frequency spectra. Shown in the right frame of the figure are the spectra of the wall-normal velocity fluctuations at the second tap location, $x/C = 0.92$. For the intermediate and smallest time steps, 0.0016 and 0.0032, Fig. 6 exhibits convergence in the higher-frequency range for values smaller than about 3000 Hz, with clearly more frequency content compared to the coarser time step of 0.0064. Consequently, the DES predictions reported next and summarized in Tables 1 and 2 were obtained using a dimensionless

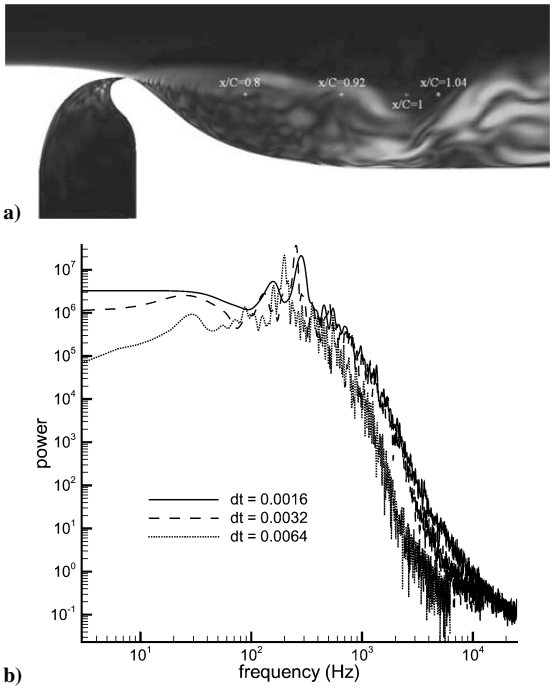

Fig. 6 Locations in the wake $x/C = 0.8$, $x/C = 0.92$, and $x/C = 1.04$ identifying positions where a) time series were extracted and b) the frequency spectra of the wall-normal velocity fluctuations at $x/C = 0.92$. The wall-normal location of each coordinate is $y/C = 0.093c$.

time step 0.0032 (4×10^{-5} s). Figure 6 also shows in the spectra a peak occurring at approximately 270 Hz, corresponding to a Strouhal number based on the hump height and freestream speed of around 0.43.

RANS predictions of the three-dimensional geometry were obtained using a series of unstructured grids with resolutions ranging from 2.59×10^6 to 10.72×10^6 cells and generated using VGRIDns.[13] These meshes were of half the tunnel geometry, that is, from the splitter plate to the upper wall, over half the spanwise extent of the lower test surface, including the endplates that are attached to the hump and with symmetry conditions imposed across the centerplane of the tunnel (indicated by the half-geometry entry in the tables). The three-dimensional RANS predictions are of the steady-state flow obtained by integrating the equations using large time steps for a CFL $= 10^6$. Tests of the time-dependent nature of the RANS flowfields were performed for a few selected cases in which the RANS equations were integrated in a time-accurate fashion. These tests showed that the time-accurate RANS predictions evolved to steady solutions.

The two-dimensional RANS predictions of the suction/blowing case were time accurate. The influence of the time step on the slot velocity is shown in Fig. 3. Results using four time steps are shown, the figure illustrating convergence in the temporal evolution of the slot velocity for a dimensionless time step of 8×10^{-4}.

IV. Results

A. Baseline and Steady-Suction Cases

Contours of the streamwise velocity normalized by the freestream speed from the S-A RANS prediction and vorticity isosurfaces from the DES prediction of the baseline case are shown in Fig. 7. Included in the RANS results are streamlines showing the recirculation zone that develops in the aft region of the hump. For the baseline case, the (steady) S-A RANS result shows that the boundary layer separates at about the location of the slot and with reattachment downstream at $x/c = 1.28$. For the case with steady suction, the streamlines indicate that the suction is not sufficient to eliminate the recirculation zone downstream of the slot, although comparison of the frames shows that the size (height and streamwise extent) of the separated region has been decreased compared to the baseline case. Reattachment

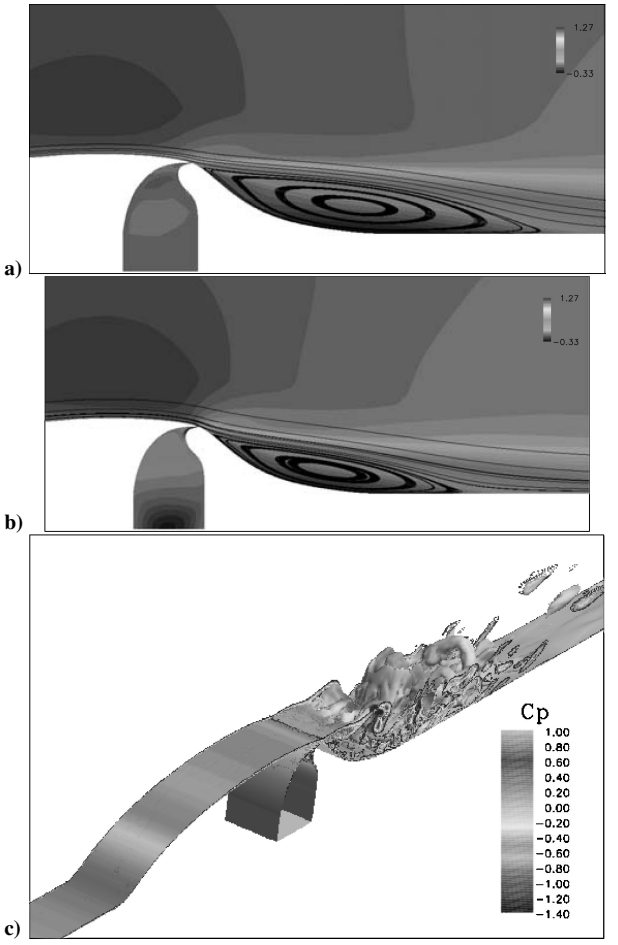

Fig. 7 Streamlines and contours of the streamwise velocity in the S-A RANS prediction of the a) baseline case and b) steady-suction case and c) vorticity isosurfaces (shaded by pressure) in the DES prediction of the baseline case.

is predicted at $x/C = 1.124$ in the two-dimensional S-A RANS. Figure 7 shows that for the DES prediction, beginning in the region downstream of the slot there is a range of eddies resolved, consistent with LES treatment of the separated region.

The pressure coefficient from predictions of the baseline and steady-suction cases is shown in Fig. 8. All two-dimensional results are compared to measurements along the channel centerplane. The RANS predictions of the two-dimensional solution are from the finest grids (841×217 cells) and from the intermediate grid for the three-dimensional solutions (4.90×10^6 cells). In forming the pressure coefficient, for the two-dimensional simulations the reference pressure was adjusted to match experimental measurements upstream of the hump leading edge. For the three-dimensional calculations the pressure coefficient was computed using the reference conditions in the freestream at $x/C = -2.14$ (the coordinate origin $x/C = 0$ is at the hump leading edge), corresponding to the same reference location as used in the experiments. The curves shown are extracted from the symmetry plane of the calculation.

For the baseline case in Fig. 8a, the experimental measurements show the development of an adverse pressure gradient upstream of the hump leading edge and a region of flow acceleration beginning near $x/C = 0$ to about $x/c = 0.5$. Downstream of $x/c = 0.5$, the pressure gradient becomes strongly adverse with boundary-layer detachment occurring near the slot ($x/C = 0.65$). The experimental measurements show the flow reattaches at $x/C = 1.11$, reattachment locations predicted by the models for the baseline and steady suction cases are summarized in Table 4.

Figure 8a shows that upstream of $x/C \approx 0.25$ the two-dimensional S-A RANS and two-dimensional SST RANS

Table 4 Reattachment locations for the baseline configuration (no flow control) and the steady-suction case

Case	Reattachment x/C (baseline)	Reattachment x/C (steady suction)
Measurements	1.11	0.94
Two-dimensional S-A	1.28	1.12
Two-dimensional SST	1.28	1.11
DES	1.13	1.10
Three-dimensional S-A	1.25	1.09
Three-dimensional SST	1.24	1.10

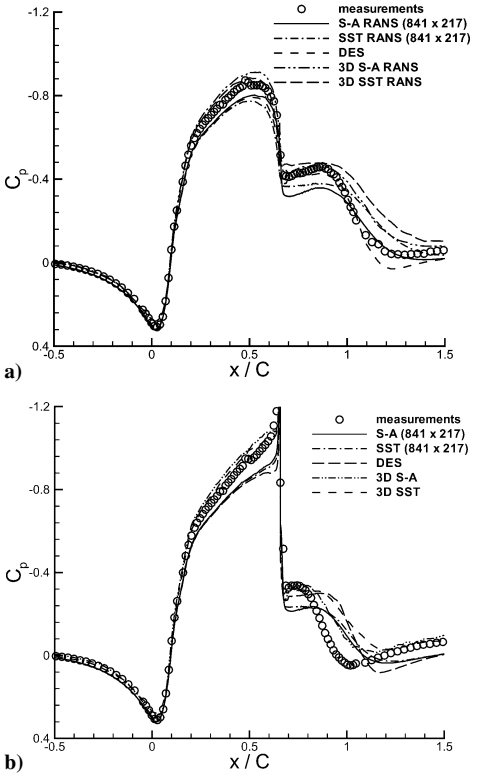

Fig. 8 Pressure coefficient predictions: a) baseline case and b) steady-suction case. Pressure coefficients from the three-dimensional RANS correspond to the symmetry plane.

predictions are essentially identical and in good agreement with the experimental measurements, reflecting comparable accuracy in predicting boundary-layer growth upstream of the hump and the region of strong acceleration over the front of the hump. The peak suction predicted by the S-A RANS in the vicinity of $x/C = 0.5$ is in closer agreement to the measurements than obtained using the SST model, although both two-dimensional RANS results are tangibly lower than the measured peak. The pressure coefficient sharply increases from $x/C \approx 0.5$ to $x/C \approx 0.65$, a feature captured by the two-dimensional RANS. Figure 8a shows the maxima near $x/C = 0.65$ predicted in the two-dimensional S-A RANS is larger than obtained using SST, with the SST prediction exhibiting better agreement with measurements near the location of boundary-layer separation. The two-dimensional RANS reattach farther downstream, at $x/C = 1.28$, than the location of mean reattachment reported in the experiments of $x/C = 1.11$ (compare to Table 4). Figure 8a shows that both of the two-dimensional RANS predictions of the pressure coefficient in the separated region (between $x/C = 0.65$ and 1.28) are shifted below the measured mean pressures. Figure 8a also shows that the recovery in the pressure coefficient following reattachment is different from that measured.

The DES prediction yields a similar pressure distribution as the two-dimensional RANS predictions to approximately the point of flow detachment, that is, up to around $x/C = 0.65$. Following boundary-layer separation, Fig. 8a shows that the DES prediction of the pressure coefficient is in better agreement with measurements than obtained using two-dimensional RANS. In addition, mean flow reattachment in the DES occurs further upstream than in the two-dimensional RANS with the DES predicting reattachment at $x/C = 1.13$. Downstream of reattachment, Fig. 8a shows an improved prediction of boundary-layer recovery using DES, though the mean pressure is slightly higher than measured for $x/C > 1.2$.

The underprediction of the peak suction near $x/C = 0.5$ by the two-dimensional RANS and DES motivated an investigation of mesh resolution, the influence of the upper-surface boundary condition, and the development of the upstream boundary layer over the lower (test) surface (compare to Table 1). For the two-dimensional RANS and DES predictions in Fig. 8a, a slip surface was imposed along the upper boundary, that is, zero tangential stress and zero surface-normal velocity. Though not shown here, the difference in the peak suction between the two-dimensional RANS and measurements could not be accounted for via changes in the upper-surface boundary condition, for example, imposing a no-slip surface and resolving the boundary layer along the upper wall and/or increases in mesh resolution.

The influence of blockage effects—arising from the wind-tunnel walls and including the endplates mounted at the ends of the hump—on the pressure distribution was investigated using solutions of the three-dimensional RANS equations. Figure 8a shows the results from the three-dimensional RANS cases, using both the S-A and SST models. As apparent in the figure, the peak suction pressure is stronger in the three-dimensional RANS compared to either the two-dimensional RANS or DES. Both three-dimensional RANS results shows good agreement with the measured distribution, a consequence of similar blockage now accounted for in the three-dimensional computation. In addition, Fig. 8a shows the pressure levels in the separated region are more accurately predicted in the three-dimensional RANS, with the S-A result in slightly better agreement with the measurements. Although the figure shows that the pressure levels predicted in the three-dimensional RANS in the vicinity $0.65 < x/C < 1$ are more accurate than in the two-dimensional RANS, reattachment occurs in nearly the same location (compare to Table 4), and Fig. 8a shows a different recovery in C_p than measured.

The pressure coefficient predicted by using the same techniques, two- and three-dimensional RANS and DES, for the steady-suction case are shown in Fig. 8b. As also observed in the baseline case, a similar adverse pressure gradient upstream of the hump is observed. For the steady-suction case, Fig. 8b shows that the peak negative pressure prior to flow detachment is higher. Similar to the behavior observed in the baseline case, the two-dimensional RANS results underpredict the peak pressure before flow detachment as a result of blockage effects in the measurements that are not taken into account in the two-dimensional RANS. It is useful to stress again that grid sizes for the three-dimensional RANS computations are sufficient such that the pressure coefficient is grid converged. Thus, the results in Fig. 8 reflect physical effects (blockage) rather than a numerical artifact caused by inadequate resolution.

As illustrated in Fig. 7, suction through the slot is not sufficient to fully attach the flow, though it does reduce the size of the recirculation region. Reattachment locations predicted by the models for the steady-suction case are also shown in Table 4. The measurements in Fig. 8b show that there is a larger increase in the pressure both just downstream of flow detachment ($x/C = 0.65$) and in the vicinity of reattachment as compared to the baseline case. The two-dimensional RANS predictions also exhibit larger pressure increases in the suction over the baseline cases, although the figure shows the overall agreement with measurements in the separated region is unsatisfactory.

The DES prediction for the steady-suction case is very similar to the two-dimensional RANS results prior to flow separation. The pressure rise following flow detachment is also in better agreement with measurements compared to the RANS, although Fig. 8b shows that the DES prediction of the steady-suction case is less accurate compared to the baseline flow in Fig. 8a. The figure shows that the variation in the pressure coefficient in the DES appears similar

to the measured distribution, though with a downstream lag, that is, toward larger x/C. In the present DES the development and growth of turbulent eddies in the separated region relies on amplification of the instabilities in the separated shear layer detaching from the hump. This process is not "instantaneous," and the lag apparent in the pressure coefficient in Fig. 8b is consistent with a delay in the development of eddies within the recirculating region, also consistent with the shallower separation compared to the baseline case.

The three-dimensional RANS predictions of the steady-suction case exhibit similar features observed for the baseline. The pressure distribution over the hump, prior to separation, is more accurately recovered than in the two-dimensional RANS or DES. Also similar to the RANS predictions of the baseline configuration, the pressure levels in the separated region are more accurate than using two-dimensional RANS, though the overall agreement with measurements for $0.65 < x/C < 1.3$ is inadequate. Note also that evidence of the blockage effects are apparent in the recovery of C_p downstream of $x/C = 1.3$ where the three-dimensional RANS predict the same pressure levels as measured and the two-dimensional RANS and DES predicting higher pressures.

Predictions and measurements of the streamwise mean velocity at four streamwise stations, $x/C = 1.0$, 1.1, 1.2, and 1.3, corresponding to locations within and slightly downstream of the separated region are shown in Fig. 9. At $x/C = 1.0$ the reverse-flow velocity very close to the wall is overpredicted using the S-A model, though there is very good agreement for $y/C > 0.02$. The peak reverse-flow velocity at $x/C = 1.0$ predicted using two-dimensional SST is closer to the measurements very near the wall though with the mean streamwise velocity underpredicted over most of the remainder of the profile. The figure shows that the DES prediction agrees very well with the measurements. With downstream evolution the two-dimensional RANS results lag the measured profile, with the S-A predictions in slightly better agreement with measurements. DES predictions are in better agreement with the experiments although they exhibit a slight lag compared to the measurements near the outer layer of the profile.

Figure 10 shows the comparison of the two-dimensional RANS and DES predictions to the measurements of the mean streamwise velocity profiles for the steady-suction case. The predictions show larger disagreement with measurements than observed in the comparisons for the baseline case, especially in the region nearest to the wall where both RANS and DES underpredict the velocity. The disagreement is anticipated based on the pressure distributions just summarized.

Figures 11 show the Reynolds shear-stress profiles for the baseline and steady-suction cases obtained using two-dimensional RANS and DES. For both the baseline and steady-suction cases the DES results in the figure show that the modeled stress is essentially zero and that all of the Reynolds stress supported by the computation is being resolved. In the baseline case at $x/C = 0.9$, the overall agreement between the DES and measurements is adequate: both the maximum and location of the peak shear stress appear reasonably predicted. The two-dimensional RANS predictions yield very similar profiles; a consistent feature for both cases and the two streamwise stations shown is the relatively low shear stress compared to the measured profile, which results in the larger separation bubble (e.g., reattachment length farther aft than measured) than indicated in the experiments. As shown in Fig. 11b, the resolved Reynolds shear stress in the DES at $x/C = 1.0$ is substantially greater than the RANS results, although also above the measured profile. For the steady-suction case, the DES prediction at $x/C = 0.9$ (Fig. 11c) does not agree as well with measurements as the corresponding profile in the baseline case: the levels are lower than measured, and the peak is farther from the wall.

B. Sinusoidal Suction/Blowing

Streamlines and contours of the streamwise velocity normalized by the freestream speed from the S-A RANS prediction of the sinusoidal suction/blowing case are shown in Fig. 12. The results shown in the figure correspond to the control case measured in experiments in which the maximum velocity through the slot during the blowing phase of the cycle was 26.6 m/s. As summarized in Table 3, this velocity corresponds to a mass flux over the entire slot of 0.0179 kg/s.

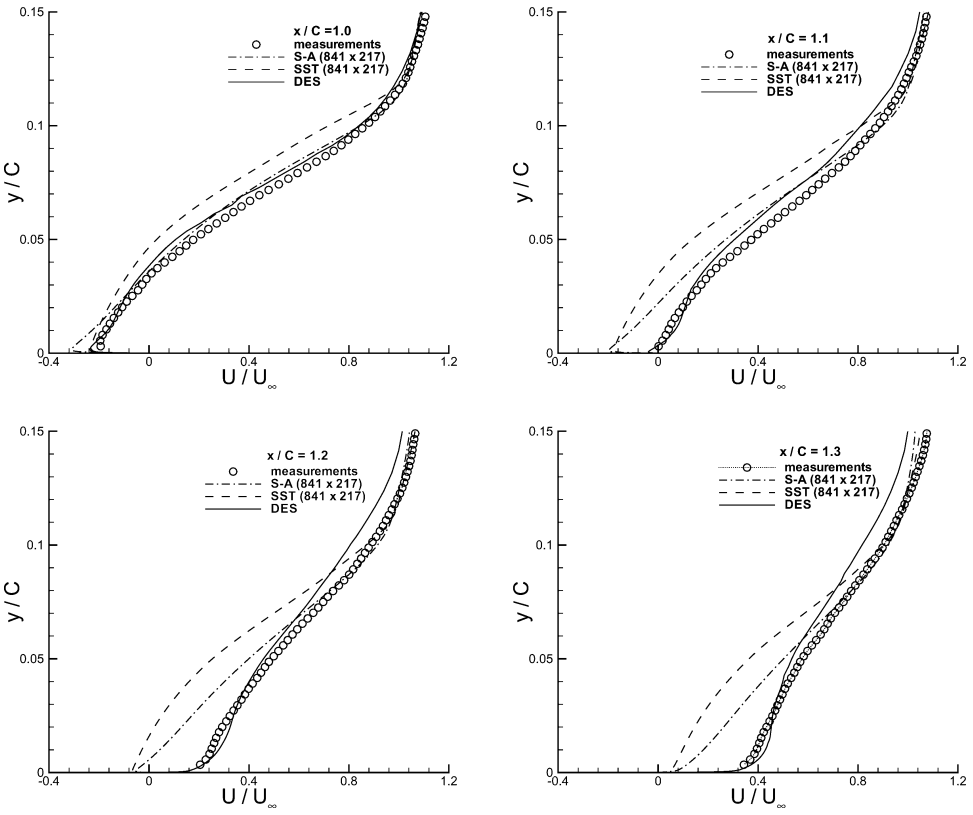

Fig. 9 Two-dimensional RANS and DES predictions of the streamwise mean velocity for the baseline case at $x/C = 1.0$, 1.1, 1.2, and 1.3.

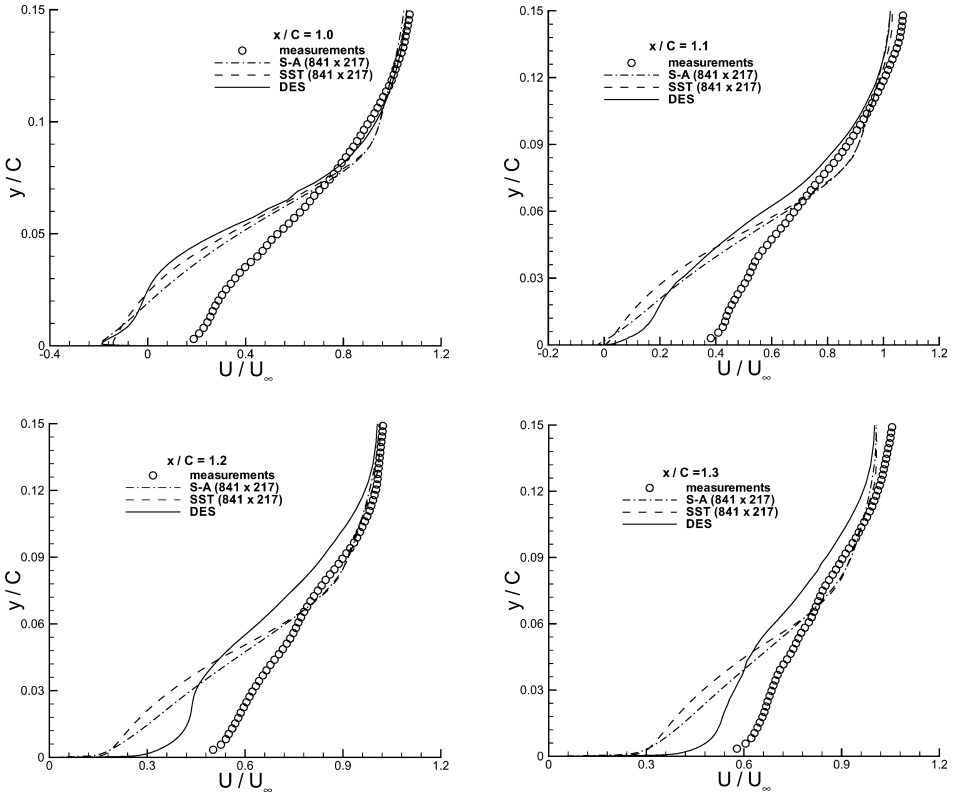

Fig. 10 Predictions of the streamwise mean velocity in the steady suction case at $x/C = 1.0$, 1.1, 1.2, and 1.3.

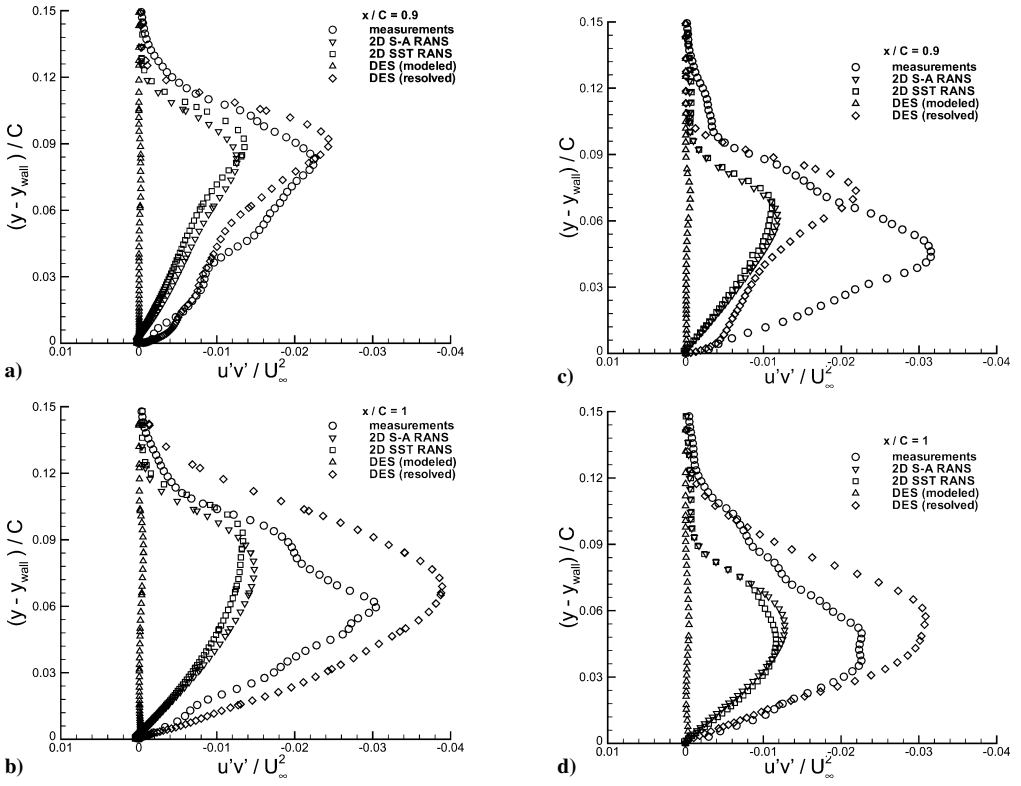

Fig. 11 Reynolds shear stress in the a, b) baseline and c, d) steady-suction cases at $x/C = 0.9$ and 1.0.

In contrast to the baseline or steady-suction cases depicted in Fig. 7, Fig. 12 shows that the influence of the suction/blowing leads to the formation of eddies, which rapidly develop from the slot and evolve downstream.

The time-averaged pressure coefficient for the case corresponding to Fig. 12 is shown in Fig. 13. The pressure distribution upstream and over the front portion of the hump, to about $x/C = 0.5$, is very similar to that measured and predicted in the baseline case (compare to Fig. 8). As already discussed, the mismatch in the peak suction between the simulations and experiments near $x/C = 0.5$ is a result of blockage effects not modeled by the two-dimensional computations. Just prior to the location of the slot ($x/C = 0.65$), there is an abrupt pressure rise that is slightly overpredicted in the calculations. The roll up of structures immediately downstream of the slot results in a secondary minima that occurs around $x/C = 0.75$ in the measurements and, less pronounced, in the RANS at around $x/C = 0.70$.

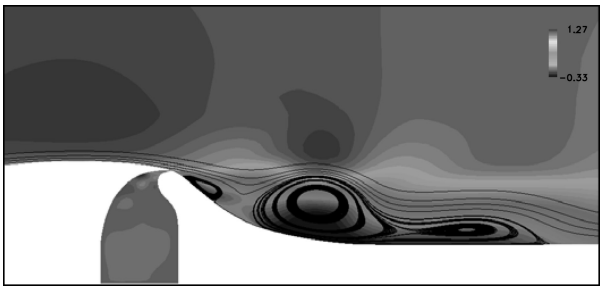

Fig. 12 Streamlines and contours of the streamwise velocity in the instantaneous solution from the S-A RANS prediction of the pulsed suction/blowing case.

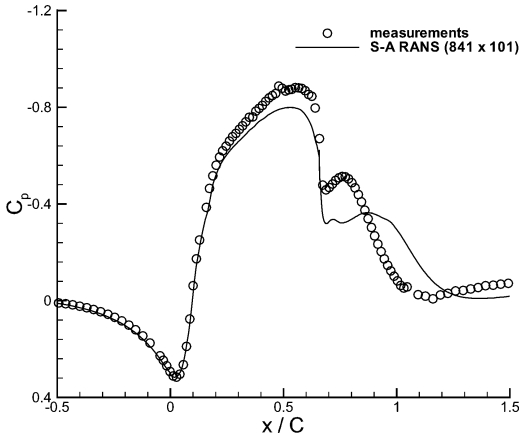

Fig. 13 Pressure coefficient predictions for sinusoidal suction/blowing case.

Analogous to the behavior observed in the two-dimensional RANS of the baseline and steady-suction cases, the predicted pressure distribution does not agree well with measurements farther downstream of the slot.

The RANS predictions of the sinusoidal suction/blowing case were also used to investigate impedance effects associated with increases in the cavity driving velocity, specified via changes in the mass flux. In the incompressible limit, the volume flux exiting the slot would be identical to the volume flux through the cavity opening. The average fluid velocity through the slot would then be dictated by the area ratio of the slot to that of the cavity. For the current ratio of the cavity area to the slot area, the average slot velocity would be approximately 70 times the cavity velocity for an incompressible fluid. Compressibility effects will introduce an impedance that will lower the volume flux relative to that which can be achieved in the incompressible limit, in turn lowering the average slot velocity, which implies a less effective control.

A series of two-dimensional S-A RANS calculations were performed to investigate impedance effects; the parameters are summarized in Table 3. The mass flux was increased by a factor of 1.5, 2, and 4 times an initial value of 0.0140 kg/s. Shown in Fig. 14 is the ratio of the average velocity through the slot $V_{\text{slot,avg}}$, during the blowing phase to the maximum driving velocity through the cavity $V_{\text{diaphragm}}$. The slot velocity has been made dimensionless using the driving velocity; the horizontal axis of Fig. 14 is nondimensionalized by the diaphragm velocity for the initial calculation corresponding to a mass flux of 0.0140 kg/s. For the initial calculation $V_{\text{diaphragm}}/V_{\text{diaphragm,initial}} = 1$, Fig. 14 shows the average slot velocity is approximately 56 times the driving velocity of the diaphragm, lower than the maximum value of 70 that would be achieved in the incompressible limit. Figure 14 shows that for increases in the driving velocity in the cavity of 1.5 and 2 times the initial value there is an approximately linear decrease in the average slot velocity. For an increase in the driving velocity by a factor of four (corresponding to a cavity mass flux of 0.0560 kg/s), the figure shows that the

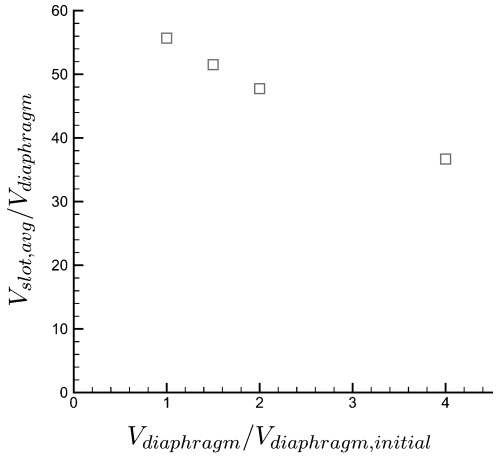

Fig. 14 Ratio of the average slot velocity to the driving (diaphragm) velocity.

average slot velocity also increases, though not by the same factor. Figure 14 shows that the average slot velocity is about 38 times the driving velocity, corresponding to an increase by a factor of only 2.7 compared to the factor-of-four increase in the driving speed.

V. Summary

RANS and DES were applied to prediction of the flow over a wall-mounted hump. The influences of grid topology, grid refinement, and the upper-surface boundary condition were investigated. RANS predictions of the two-dimensional flow using structured or unstructured grids and over a reasonable range of grid refinement exhibited insignificant changes. The two-dimensional RANS predictions were not appreciably altered with changes in the upper-surface boundary condition. The main motivation for investigations of the upper-surface boundary condition arose from the mismatch in the peak suction pressure near the top of the hump, which was underestimated in the two-dimensional RANS as well as the DES. The larger suction in the experimental measurements of the pressure distribution was more accurately recovered using three-dimensional RANS computations that accounted for blockage effects arising from the wind-tunnel walls and the endplates attached to the hump. Tailoring the upper wall-pressure distribution by adjusting the shape of the top wall would enable two-dimensional computations to account for blockage, as reported in Rumsey et al.[6]

For the baseline configuration (no flow control), the two-dimensional RANS overpredicts the mean pressure in the separation zone. Comparison to the three-dimensional RANS results shows that the two-dimensional predictions are nearly a shift of the three-dimensional pressure distributions, failing to account for the confining effects of the wind-tunnel walls that are more accurately captured in the three-dimensional RANS. The DES predictions of the baseline configuration were encouraging: the three-dimensional structure resolved in the wake improved the physical description of the flow in the separated region and the quantitative prediction of the mean pressure distribution and mean streamwise velocity. For the flow with steady suction, the two- and three-dimensional RANS yielded different predictions again caused by different blockage effects.

DES predictions in the present investigations were obtained on a single grid; additional computations on finer meshes were beyond the scope of the current investigations, although they would be essential to a deeper examination of the technique in the current flow. One drawback of the DES as employed here is that the RANS region was maintained to the location of the slot, an undesirable feature in practice though compatible with the primary objectives of the work to gauge the feasibility and to provide an initial assessment of the accuracy of the approach for a complex configuration directly relevant to flow control. Nevertheless, improvements to the technique

are required in order to exert more control over the RANS–LES interface than is currently possible using the grid.

In spite of using only a single mesh, grid design was guided based on experience acquired in computation of other flows, for example, attempting to ensure nominally cubic cells in the focus region (separated region downstream of the slot), and choosing the time step to yield a CFL of about unity based on the grid dimensions in the focus region. A complicating factor for flow control applications and relevant to the current study is that, although CFL numbers in the separated region downstream of the hump were $\mathcal{O}(1)$, CFL numbers near the slot are substantially larger. An accurate LES treatment of the flow that includes the slot region would require much smaller time steps than considered in the present computations. An additional issue for flow control applications is treatment of the cavity. In the present effort the flow within the cavity was modeled, rather than prescribing a jet velocity at the slot opening. For relatively small values of the cavity mass flux, a prescribed jet velocity would be a useful simplification, although for higher mass flux impedance effects become significant and a prescribed slot velocity could be quite different from the actual conditions of the flow exiting the slot.

Although DES predictions of the baseline configuration were encouraging, there was disagreement with experimental measurements for the steady-suction case, which did not recover the pressure distribution nor the mean streamwise velocity in the separated region to similar accuracy. The current configuration does not belong to the class of massively separated flows for which the technique was originally designed. The relatively more shallow separation as compared to the baseline configuration poses a strong challenge to hybrid RANS–LES methods and highlights the need for incorporation into the simulations of strategies to seed upstream eddy content into the boundary layer, in regions where the boundary-layer grid is sufficient to support eddies. The degree to which DES predictions would be improved by such a procedure poses an interesting question, one that deserves further investigations.

Two-dimensional unsteady RANS was also used to predict the case with sinusoidal suction/blowing, the solutions exhibiting a time-dependent shedding of vortical structures. That the mean pressure distribution did not exhibit good agreement with measurements again provides impetus for continued development and application of techniques such as DES. The two-dimensional unsteady RANS were used to investigate impedance effects associated with increases in the driving force, that is, mass flux (velocity) through the cavity opening. A factor-of-four increase in the cavity mass flux resulted in an increase of the average velocity through the slot by only a factor of 2.7, an important result given the less efficient control that would likely result with increases in the driving force.

Acknowledgments

The authors gratefully acknowledge the support of the Air Force Office of Scientific Research (Grant F49620-02-1-0117; Program Officer, Thomas Beutner) and discussions with Philippe Spalart. The work was performed as part of a U.S. Department of Defense Challenge project at the Aeronautical Systems Center Major Shared Resource Center and the Maui High Performance Computing Center.

References

[1]Seifert, A. and Pack, L. G., "Active Control of Separated Flows on Generic Configurations at High Reynolds Numbers," AIAA Paper 99-3403, 1999.

[2]Seifert, A., Darabi, A., and Wygnanski, I., "Delay of Airfoil Stall by Periodic Excitation,"*Journal of Aircraft*, Vol. 33, No. 4, 1996, pp. 691–699.

[3]Seifert, A., and Pack, L. G., "Oscillatory Control of Separation at High Reynolds Numbers," *AIAA Journal*, Vol. 37, No. 9, 1999, pp. 1062–1071.

[4]Spalart, P. R., Jou, W.-H., Strelets, M., and Allmaras, S. R., "Comments on the Feasibility of LES for Wings, and on a Hybrid RANS/LES Approach," *Advances in DNS/LES, 1st AFOSR International Conference on DNS/LES*, Greyden Press, Columbus, OH, 1997.

[5]Squires, K. D., "Detached-Eddy Simulation: Current Status and Perspectives," *Direct and Large-Eddy Simulation V*, edited by R. Friedrich, B. J. Geurts, and O. Metais, Kluwer Academic, Dordrecht, The Netherlands, 2004, pp. 465–480.

[6]Rumsey, C., Gatski, T., Sellers, W., Vatsa, V., and Viken, S.,"Summary of the 2004 CFD Validation Workshop on Synthetic Jets and Turbulent Separation Control," AIAA Paper 2004-2217, 2004.

[7]Spalart, P. R., and Allmaras, S. R., "A One-Equation Turbulence Model for Aerodynamic Flows," *La Recherche Aerospatiale*, Vol. 1, 1994, pp. 5–21.

[8]Menter, F. R., "Two-Equation Eddy-Viscosity Turbulence Models for Engineering Applications," *AIAA Journal*, Vol. 32, No. 8, 1994, pp. 1598–1605.

[9]Strang, W. Z., Tomaro, R. F., and Grismer, M. J., "The Defining Methods of Cobalt_{60}: A Parallel, Implicit, Unstructured Euler/Navier–Stokes Flow Solver," AIAA Paper 99-0786, 1999.

[10]Gottlieb, J. J., and Groth, C. P., "Assessment of Riemann Solvers for Unsteady One-Dimensional Inviscid Flows of Perfect Gases," *Journal of Computational Physics*, Vol. 78, No. 2, 1988, pp. 437–458.

[11]Karypis, G., Schloegel, K., and Kumar, V., "ParMETIS: Parallel Graph Partitioning and Sparse Matrix Ordering Library," Ver. 1.0, Dept. of Computer Science, Univ. of Minnesota, Minneapolis, MN, July 1997.

[12]Spalart, P. R., "Young-Person's Guide to Detached-Eddy Simulations Grids," NASA CR-2001-211032, 2001.

[13]Pirzadeh, S., "Three-Dimensional Unstructured Viscous Grids by the Advancing-Layers Method," *AIAA Journal*, Vol. 34, No. 1, 1996, pp. 43–49.

C. Rumsey
Guest Editor